

# Kinematic Glacier Thickness Inversion Using 3-D Flow Velocities From Multitrack SAR Images

Liyue Yang<sup>ID</sup>, Zhong Lu, *Senior Member, IEEE*, Chaoying Zhao<sup>ID</sup>, *Senior Member, IEEE*, Xie Hu<sup>ID</sup>, *Senior Member, IEEE*, and Baohang Wang<sup>ID</sup>

**Abstract**—Accurate estimation of glacier thickness across space and time is essential for understanding glacier dynamics and their response to climate change. Traditional approaches are often constrained by uncertainties arising from dependence on poorly understood physical parameters. In this study, we develop a remote-sensing-based framework for glacier thickness inversion using multitrack synthetic aperture radar observations. Three-dimensional displacement time series of the Jiongpu glacier in High Mountain Asia were generated from Sentinel-1 imagery acquired between 2019 and 2022 using a pixel offset multidimensional small baseline subsets technique. These velocity fields were combined with surface mass balance to invert glacier thickness through a Monte Carlo approach, in which the rheological parameter was adaptively optimized based on terrain slope and horizontal velocity. Sensitivity analyses demonstrate that rheological parameter optimization reduces uncertainty by up to 18.4% in standard deviation and 20.4% in coefficient of variation compared with fixed values, while the inclusion of vertical velocity further decreases variation by 42.1%. Perturbations of slope by plus or minus 2.0 degrees increase thickness uncertainty by as much as 6.08 m. Thickness change estimates along a transect show strong agreement with elevation change from ICESat-2, with a correlation coefficient of 0.91. These findings confirm that the proposed framework effectively captures the spatiotemporal variability of glacier thickness and reduces inversion uncertainty, providing a robust and scalable approach for monitoring glacier evolution and associated hazards in data-scarce mountainous regions.

**Index Terms**—Glacier 3-D velocities, glacier thickness, high-mountain Asia, multitrack SAR images, pixel offset tracking and multidimensional small baseline subset (PO-MSBAS).

Received 23 January 2025; revised 23 April 2025, 5 June 2025, and 21 August 2025; accepted 13 October 2025. Date of publication 24 October 2025; date of current version 7 November 2025. This work was supported in part by the National Natural Science Foundation of China under Grant 42474029 and in part by the Scientific Research Foundation for Young Scholars of Xiangtan University under Grant KZ0807569. (*Corresponding author*: Chaoying Zhao.)

Liyue Yang is with the College of Civil Engineering, Xiangtan University, Xiangtan 411105, China, and also with the Hunan Provincial Key Laboratory of Geomechanics and Engineering Safety, Xiangtan University, Xiangtan 411105, China (e-mail: liyue\_yang@xtu.edu.cn).

Zhong Lu is with the Roy M. Huffington Department of Earth Sciences, Southern Methodist University, Dallas, TX 75275 USA, and also with the School of Environment and Spatial Informatics, China University of Mining and Technology, Xuzhou 221008, China (e-mail: zhonglu@mail.smu.cn).

Chaoying Zhao is with the School of Geological Engineering and Geomatics, Chang'an University, Xi'an 710054, China (e-mail: cyzhao@chd.edu.cn).

Xie Hu is with the College of Urban and Environmental Sciences, Peking University, Beijing 100101, China (e-mail: hu.xie@pku.edu.cn).

Baohang Wang is with the College of Geography and Oceanography, Minjiang University, Fuzhou 350108, China (e-mail: wangbaohang@mju.edu.cn).

Digital Object Identifier 10.1109/JSTARS.2025.3624258

## I. INTRODUCTION

THE ice thickness distribution of glaciers is a fundamental parameter for many glaciological applications [1], [2]. Modeling glacier thickness is important because it allows assessing long-term changes in glaciers and simulating glacial lake outburst floods (GLOF) caused by glacial avalanches moving into lakes [3], [4], [5]. Estimating glacier thickness contributes to more accurate assessments of ice loss [6], [7]. Currently, glacier melt accounts for 25%–30% of sea level rise [8]. Despite the importance of glacier thickness, direct measurements of glacier thickness are limited due to the complex mountainous topography of the high-mountain area (HMA). Conventional measurement techniques, including radio-echo sounding or borehole measurements, are expensive and laborious-intensive.

International efforts over the past few decades have significantly improved the representation of glacier thickness [1], [2], [3], [9], [10]. The simplest method, known as the scaling method, investigates the relationships between glacier area and volume. This approach provides an estimate of the average ice thickness for a glacier [11], [12], [13]. Other glacier thickness models mostly use simplified glacier geometries based on the width-averaged centerline approach and make strong assumptions about basal shear stress or surface mass balance gradients [14]. Currently, models for estimating glacier thickness have developed from theoretical considerations [15], [16], [17] to neural network approaches [18], [19]. This leads to a situation where, although many methods are available, they often have low applicability and spatial resolution due to the lack of many physical parameters (e.g., basal shear, rate of thickness change, and basal velocity). These models rely on multiple datasets, are sensitive to the quality of the input data, and are less applicable to other mountain glaciers.

Glacier flow defines ice transfer and largely controls the spatial distribution of ice volume [20]. As an important constraint for glacier thickness modeling, mapping glacier flow remains relatively difficult due to the limited availability of optical images with sufficient quality and resolution. With the launch of multiple synthetic aperture radar (SAR) systems over the past decade, high spatiotemporal resolution observations have opened up new opportunities for mapping the ice-flow velocities in Earth's glaciers [20], [21]. The amplitude-based pixel offset tracking method works well, overcoming inclement weather conditions and loss of coherence from optical feature-tracking and InSAR methods [22], [23]. The SAR offset tracking method

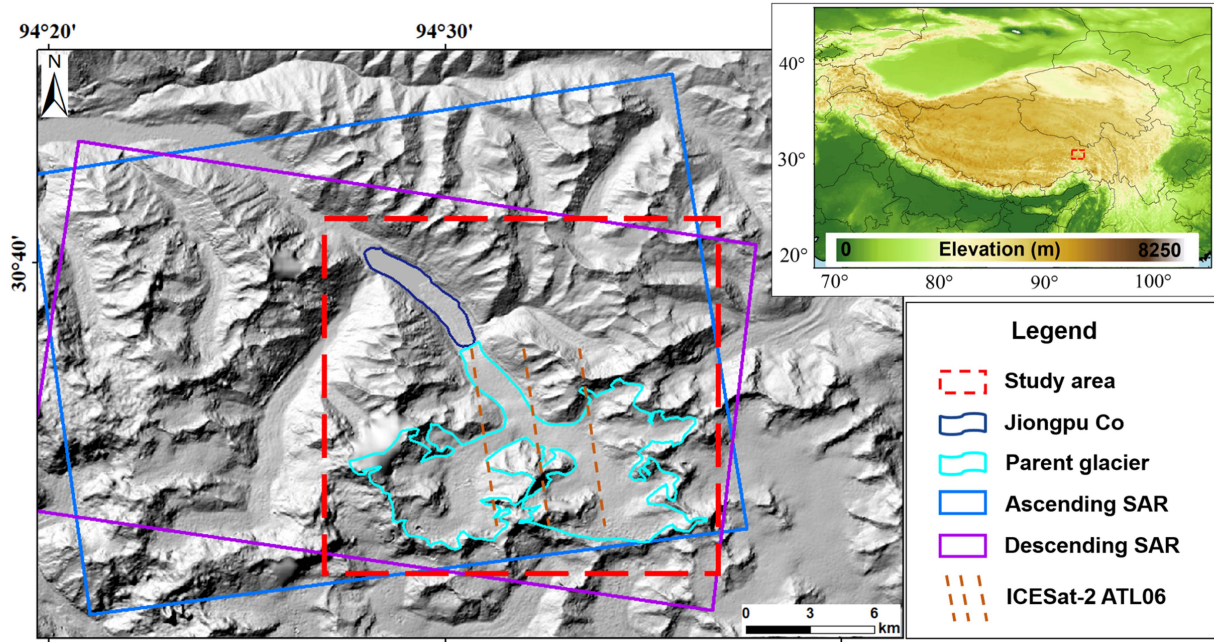


Fig. 1. Overview of the study area showing the Jiongpu Co and its parent glacier.

estimates glacier velocities in both line-of-sight (LOS) and azimuth directions [22], [24]. Moreover, real three-dimensional (3-D) flow velocities of glaciers can be retrieved based on ascending and descending SAR images [25], [26]. Obtaining full 3-D glacier velocities is significant, as it provides essential measurements for estimating glacier thickness, evaluating potential glacier avalanches, and simulating GLOF hazard chains [4], [5], [23].

In this study, we present the thickness method based on 3-D glacier velocities using noncontact remote sensing data. We apply this approach to the Jiongpu glacier in the HMA region, which has undergone the most significant mass loss in the Eastern Nyainqntanglha range [27], [28]. Following an introduction to the study area, we describe the inversion framework in detail. The method establishes a relationship between 3-D glacier velocities and ice thickness based on the principle of mass conservation. The 3-D velocity fields are derived from multitrack SAR observations. The rheological parameter is optimized based on horizontal velocity and terrain slope. We then present the results of glacier 3-D velocities and the inversion of glacier thickness. To assess the sensitivity of the inversion, we conduct a Monte Carlo-based uncertainty analysis, focusing on the impacts of variable rheological parameters, time-dependent ice velocity fields, and slope change. Finally, to evaluate the robustness of our inversion results, we compared the modeled thickness change rates over different time periods with the elevation change rates derived from Ice, Cloud, and land Elevation Satellite 2 (ICESat-2) datasets. While ICESat-2 provides elevation changes rather than direct ice thickness measurements, this comparison allows us to assess the spatiotemporal consistency of our results, thereby supporting the reliability of the method. The methodology in our study demonstrates clear advantages in producing spatiotemporal glacier thickness estimates with quantified uncertainty, and it

holds potential for application to other data-sparse mountainous glaciers.

## II. STUDY AREA AND ITS IMPORTANCE

The parent glacier for Jiongpu lake is located in southeastern Tibet, as shown in Fig. 1. Glacial melt in this area is an essential source of water for several major rivers in South and Southeast Asia [29]. The study area experiences the longest annual rainy season across the entire Tibetan Plateau, primarily due to the intrusion of the South Asian monsoon through the Grand Bend of the Yarlung Zangbo River [30], [31]. The average annual temperature is 9.0 °C. January is the coldest month with a mean temperature of 0.3 °C, and July is the hottest month, with a mean temperature of 16.7 °C [30], [31]. The rainy season in the study area typically lasts nearly seven months, from March to October, with over 80% of annual precipitation occurring between June and September. These months receive the highest amount of rainfall and contribute significantly to the overall precipitation in the region [30], [31].

Few studies have investigated glacier mass loss and lake expansion in Jiongpu lake [27], [32]. Li et al. [32] reported that the lake area expanded from  $1.19 \pm 0.09 \text{ km}^2$  to  $5.34 \pm 0.07 \text{ km}^2$ , resulting in a subaqueous equivalent ice loss of  $0.26 \pm 0.12 \text{ Gt}$  over 20 years. Zhang et al. [27] indicated that Jiongpu lake experienced the largest volume increase from 2000 to 2020. Its growth rate of  $0.29 \pm 0.18 \text{ km}^3$  per decade was the highest rate observed in the Eastern Nyainqntanglha range. During the same period, the mass loss of the Jiongpu glacier was  $0.26 \pm 0.12 \text{ Gt}$ , which exceeded 0.2 Gt, making it one of the glaciers with the largest estimated mass loss in Tibet [27], [31]. However, there is a lack of studies on multidimensional glacier velocities and thickness for the Jiongpu glacier. Understanding the ice thickness of the Jiongpu glacier is essential for

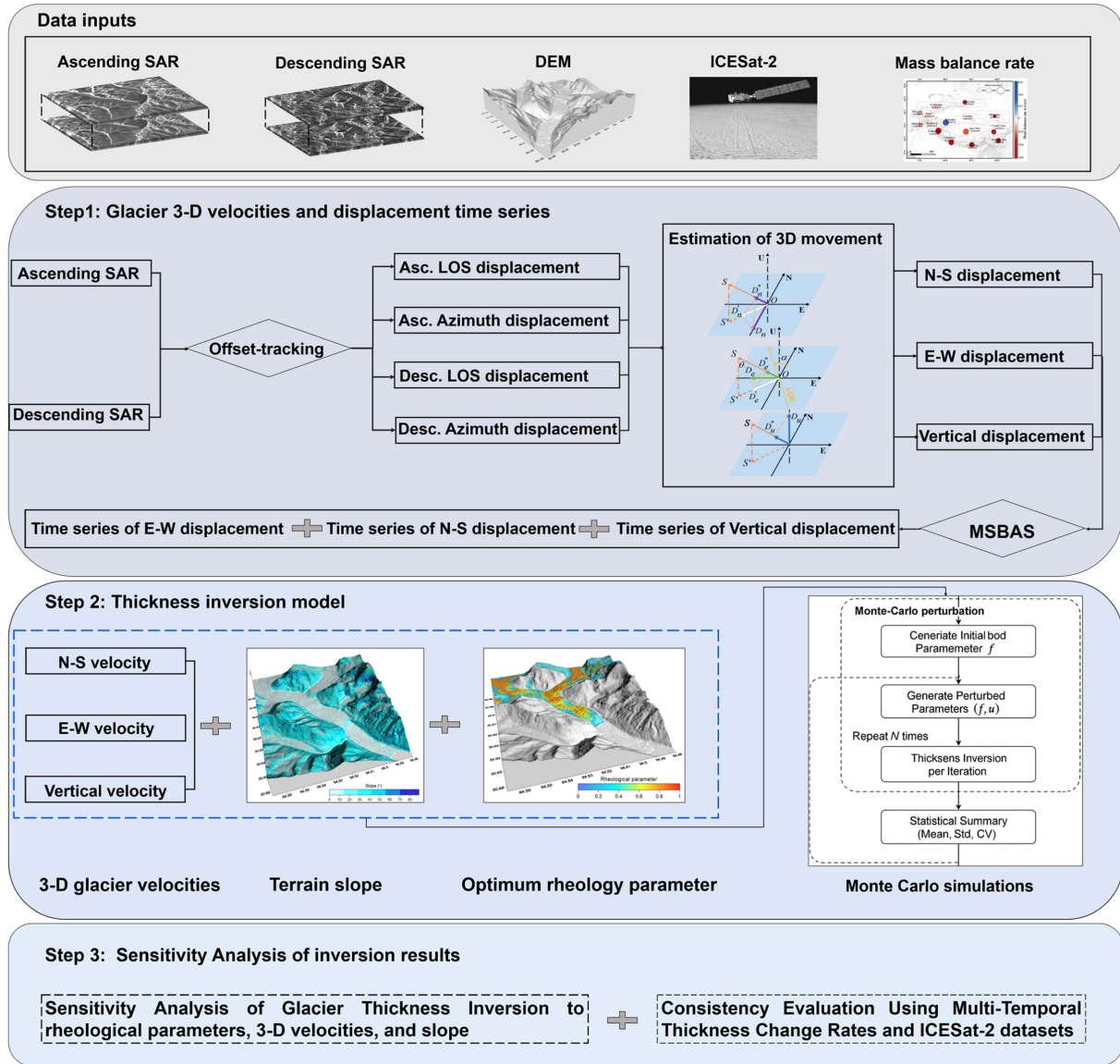


Fig. 2. Flowchart of glacier thickness inversion and uncertainty analysis.

evaluating its potential threat associated with GLOF hazards. Therefore, we integrated multisource remote sensing datasets, including ascending and descending Sentinel-1 SAR images, digital elevation model (DEM) datasets, ICESat-2 datasets, and mass balance rate, to monitor glacier 3-D velocities and thickness.

### III. DATA AND METHODS

We designed a comprehensive remote sensing method to retrieve the 3-D glacier velocities and thickness using SAR images, DEM, ICESat-2 datasets, and mass balance rate, as illustrated in Fig. 2. First, the glacier displacement in azimuth and LOS directions of ascending and descending Sentinel-1 SAR images was estimated using the SAR offset tracking method. For this study, we used Sentinel-1A SAR imagery in the Interferometric Wide swath mode, with a spatial resolution of approximately 5 m (range)  $\times$  20 m (azimuth). The polarization mode was

VV. The incidence angle was about 34° for both ascending and descending passes, while the azimuth heading angles were  $-13^\circ$  for the ascending track and  $-170^\circ$  for the descending track.

We selected the shuttle radar topography mission (SRTM) DEM for its global coverage and extensive use in remote regions. It was used for the coregistration of the multitemporal SAR images [22], [23]. Then, we retrieved the 3-D flow velocities and displacement time series from the azimuth and LOS displacements based on multitrack SAR pixel offset tracking and multidimensional small baseline subsets (PO-MSBAS) method [23], [25]. Moreover, we determined the optimum rheological parameter  $f$ , which characterizes the flow behavior of the glacier, by analyzing the ratio between terrain slope and glacier horizontal velocity. For slope estimation, we selected the advanced land observing satellite (ALOS) phased array type L-band synthetic aperture radar (PALSAR) DEM (ALOS PALSAR DEM) because it offers sufficient spatial coverage

and appropriate resolution for our study area. We compared the glacier surface slopes derived from the ALOS PALSAR DEM and the Copernicus DEM. The results showed negligible differences between the two products over glacier surfaces, indicating that the use of the ALOS PALSAR DEM does not compromise the accuracy of slope-dependent glacier thickness inversion.

To address input uncertainties and improve model robustness, we implemented a probabilistic inversion strategy based on Monte Carlo simulations for solving the mass conservation equation. This approach enabled not only accurate glacier thickness estimations but also quantified their associated uncertainties, including a detailed sensitivity analysis of the inversion results with respect to rheological parameters, time-variable 3-D velocity, and slope changes. Finally, we conducted a consistency evaluation by comparing the multitemporal thickness change rates and the elevation changes derived from ICESat-2 datasets. These analyses help assess the robustness and reliability of the inversion results. The methodology and datasets used are described in detail below.

#### A. 3-D Velocities and Displacement Time Series With Multitrack SAR Images

*1) Offset Tracking:* For the Jiongpu glacier, 74 Sentinel-1 SAR images with ascending tracks and 49 Sentinel-1 SAR images with descending tracks from January 2019 to December 2021 were collected and processed to obtain multidimensional glacier velocities. First, we derived glacier displacement along the LOS and azimuth directions from ascending and descending Sentinel-1 SAR images, respectively, using offset tracking techniques. The thresholds of the temporal and spatial baselines were set to 60 days and 200 m, respectively, to generate offset pairs while minimizing decorrelation and coregistration error caused by the glacier's rapid surface motion [31]. As a result, we formed 250 ascending image pairs (one subset) and 123 descending image pairs (three subsets). However, due to gaps in image acquisitions within the descending Sentinel-1 SAR dataset, the small baseline subset network was discontinuous.

Offset-tracking was implemented using GAMMA software, which utilized the normalized cross-correlation coefficient to

track offsets between SAR images [22], [24]. A matching window size of  $128 \times 128$  pixels (range  $\times$  azimuth) and a search step of  $4 \times 1$  pixels (range  $\times$  azimuth) were adopted to balance offset detection accuracy with the presence of outliers. The spatial resolution of offset fields is about 20 m. We used a correlation coefficient threshold of 0.3 to eliminate unreliable offsets. The 1-arc-second SRTM DEM was used to assist the image coregistration. Offsets in both azimuth and LOS directions were geocoded into the WGS84 coordinate system. To ensure spatial consistency, the ascending offset maps were resampled to match the dimensions of the descending offset maps, so that both sets shared the same grid size and spatial extent. Finally, displacements in four directions, including ascending LOS, ascending azimuth, descending LOS, and descending azimuth, were obtained to retrieve the 3-D glacier velocities and displacement time series.

*2) Estimation of 3-D Velocity and Displacement Time Series:* The multidimensional small baseline subsets (MSBAS) technique was used to retrieve 2-D displacement time series from interferometric phase observations [33], [34]. In this study, the PO-MSBAS method was employed to obtain 3-D displacement time series of glaciers. The pixel-offset observations were used as inputs for the MSBAS model. Using four displacement observations from ascending and descending SAR images, the 3-D displacement field can be obtained using the formulas given in the following equation (1), shown at the bottom of this page, [23], [25]: where  $D_E$ ,  $D_N$ , and  $D_U$  refer to the displacement in east, north, and vertical directions, respectively.  $A$  represents the ascending track,  $D$  indicates the descending track;  $\theta$  represents the incidence angle;  $\alpha$  represents the flight azimuth angle.  $D_{\text{los}}^A$ ,  $D_{\text{los}}^D$ ,  $D_{az}^A$ , and  $D_{az}^D$  represent the LOS displacement of ascending SAR images, LOS displacement of descending SAR images, azimuth displacement of ascending SAR images, and azimuth displacement of descending SAR images, respectively.

The functional model for retrieving the 3-D displacement from the observed pixel offsets in four directions was built up. The matrix form is as (2) shown at the bottom of this page, where  $B$  is a design matrix composing imaging geometry parameters.  $X$  is a matrix representing the east, north, and vertical glacier displacement.  $L$  is observation matrix containing the displacements in four directions. Equation (2) can be solved by singular

$$\begin{cases} D_{\text{los}}^A = D_N \sin \theta^A \cos(\alpha^A - \frac{3\pi}{2}) + D_E \sin \theta^A \sin(\alpha^A - \frac{3\pi}{2}) - D_U \cos \theta^A \\ D_{\text{los}}^D = D_N \sin \theta^D \cos(\alpha^D - \frac{3\pi}{2}) + D_E \sin \theta^D \sin(\alpha^D - \frac{3\pi}{2}) - D_U \cos \theta^D \\ D_{az}^A = D_N \sin(\alpha^A - \frac{3\pi}{2}) - D_E \cos(\alpha^A - \frac{3\pi}{2}) \\ D_{az}^D = D_N \sin(\alpha^D - \frac{3\pi}{2}) - D_E \cos(\alpha^D - \frac{3\pi}{2}) \end{cases} \quad (1)$$

$$\underbrace{\begin{bmatrix} \sin \theta^A \sin(\alpha^A - \frac{3\pi}{2}) & \sin \theta^A \cos(\alpha^A - \frac{3\pi}{2}) & -\cos \theta^A \\ \sin \theta^D \sin(\alpha^D - \frac{3\pi}{2}) & \sin \theta^D \cos(\alpha^D - \frac{3\pi}{2}) & -\cos \theta^D \\ -\cos(\alpha^A - \frac{3\pi}{2}) & \sin(\alpha^A - \frac{3\pi}{2}) & 0 \\ -\cos(\alpha^D - \frac{3\pi}{2}) & \sin(\alpha^D - \frac{3\pi}{2}) & 0 \end{bmatrix}}_B \underbrace{\begin{bmatrix} D_E \\ D_N \\ D_U \end{bmatrix}}_X = \underbrace{\begin{bmatrix} D_{\text{los}}^A \\ D_{\text{los}}^D \\ D_{az}^A \\ D_{az}^D \end{bmatrix}}_L \quad (2)$$

value decomposition to obtain the 3-D glacier velocities and displacement time series.

### B. Thickness Inversion Based on 3-D Glacier Velocities

In our study, we integrated the 3-D glacier velocities, including horizontal and vertical velocity, to infer the glacier thickness. Previous studies [1], [10], [35], [36] suggested that glaciers can be treated as incompressible media. The glacier thickness can be expressed as the divergence of ice flux and the local mass balance rate

$$\frac{\partial H}{\partial t} = -\nabla \cdot (\bar{u}H) + M \quad (3)$$

where  $\frac{\partial H}{\partial t}$  is the change in glacier thickness.  $\bar{u}$  is the depth-averaged glacier velocity.  $H$  is the glacier thickness.  $M$  is the local mass balance rate (m/yr ice equivalent, positive for accumulation, negative for ablation). We collected the local averaged mass balance rate in our study area during the same period through geodetic methods in previous studies, which indicated annual glacier mass changes of  $-0.7$ ,  $-0.4$ ,  $-0.1$  m.w.e in 2019, 2020, and 2021, respectively [7], [37].

To better understand the relationship between the depth-averaged velocity and surface velocity, we introduce the rheological parameter  $f$ , which is defined as:  $\bar{u} = fu_{\text{surf}}$ , where  $u_{\text{surf}}$  is the surface horizontal velocity, and  $f$  represents rheology parameter, a constant between 0 and 1 [10], [20].

Then, in this study, the glacier thickness change rate was approximated using the vertical velocity at the glacier surface, due to the lack of direct measurements at the glacier base. Previous studies [15], [35] have demonstrated that this approximation introduces negligible uncertainty in thickness inversion

$$\frac{\partial z}{\partial t} = -\nabla \cdot (fu_{\text{surf}}H) + M \quad (4)$$

where  $\frac{\partial z}{\partial t}$  shows vertical velocity derived from multitrack SAR measurements. Then, the method can be expressed as

$$\nabla \cdot (fu_{\text{surf}}H) = \tilde{M} \quad (5)$$

where  $f$  represents rheological parameters.  $u_{\text{surf}}$  represents horizontal velocities, which is calculated by combining north-south and east-west velocities.  $H$  represents glacier thickness.  $\tilde{M} = M - \frac{\partial z}{\partial t}$  represents glacier mass balance rate and vertical velocity. The mass balance term  $\tilde{M}$  incorporates both surface mass balance and vertical velocity components. The rheological parameter is known input, while the glacier thickness  $H$  is the unknown variable. The divergence term  $\nabla \cdot (fu_{\text{surf}}H)$  is approximated using a finite difference scheme on a regular grid. To solve for glacier thickness, we implemented an iterative relaxation method, updating thickness values until the residuals met convergence criteria. Similar iterative approaches have been employed in glacier modeling studies to approximate steady-state solutions under mass-conservation constraints [38], [39].

### C. Choice of the Optimum Rheological Parameter

The glacier thickness estimated by our method is sensitive to the choice of the rheological parameter, which essentially

serves as a scaling factor. Previous studies [1], [10] [35], [36] suggested that specific values of this parameter correspond to different flow regimes:  $f = 1/2$  is consistent with a linear vertical velocity profile,  $f = 2/3$  represents Newtonian viscous flow,  $2/3 < f < 1$  represents plug flow, and  $f = 1$  represents rigid sliding block. For landslides involving viscoplastic material, the rheological parameter is bound between  $2/3$  and  $1$ . For clay-rich landslides, the value of  $f \approx 0.8 \pm 0.09$  are estimated from global inclinometer data [39]. For glaciers, depth-averaged velocities may be up to 15% lower than surface velocities in some areas where basal ice is frozen to the bedrock [10], [20], [41]. Overall, the selection of the rheological parameter in existing literature is often based on empirical values [42], [43]. It is also common practice to assign a single, uniform rheological value across an entire glacier, without accounting for potential spatial variability at the glacier surface.

To further mitigate the effect of rheological uncertainty, we employed a parameterization approach based on glacier horizontal velocity and surface slope [20]. When the slope is nearly flat, glacier thickness tends to be overestimated. Similarly, surge-type glaciers, which exhibit high velocities, can also result in thickness overestimation [20]. Therefore, we used the ratio between surface slope and horizontal velocity of the glacier to determine the optimum rheological parameter.

First, the horizontal velocity on the Jiongpu glacier was calculated by combining the north-south and east-west components from SAR-derived 3-D velocities. Then, we obtained the terrain slope on the Jiongpu glacier through the ALOS PALSAR DEM of 12.5 m. Thereafter, we calculated the ratio between the slope and the horizontal velocity of the Jiongpu glacier. Based on previous studies [10], [20], [38], when the ratio exceeds the threshold of 0.001, the rheological parameter  $f$  is gradually increased from 0.1 to 0.4, indicating that internal deformation plays a dominant role in glacier motion. Conversely, when the ratio is below 0.001, the parameter  $f$  is gradually decreased from 0.9 down to 0.6, reflecting a regime dominated by basal sliding or low-deformation conditions.

To derive spatially-varying rheological parameters  $f$ , we used a piecewise linear mapping based on the ratio between glacier surface slope and horizontal velocity, denoted as  $R = \text{slope}/u_{\text{surf}}$ . The piecewise mapping is defined as

$$f(R) = \begin{cases} 0.1 + (0.4 - 0.1) \frac{R - R_0}{R_{\max} - R_0}, & R \geq R_0 \\ 0.9 - (0.9 - 0.6) \frac{R}{R_0}, & R < R_0 \end{cases} \quad (6)$$

where  $R_0 = 0.001$  is the threshold, and  $R_{\max}$  is the maximum value of  $R$  across the glacier domain. Therefore, instead of using a single empirical value for the entire Jiongpu glacier, we calculated spatially varying values of the rheological parameter  $f$ . This approach allowed us to determine the optimum thickness of the glacier using the optimized value of  $f$ .

### D. Uncertainties Analysis of Thickness Results

To estimate the uncertainty of glacier thickness inversion, we employed a Monte Carlo simulation instead of relying on error propagation. This method is particularly suitable for remote or

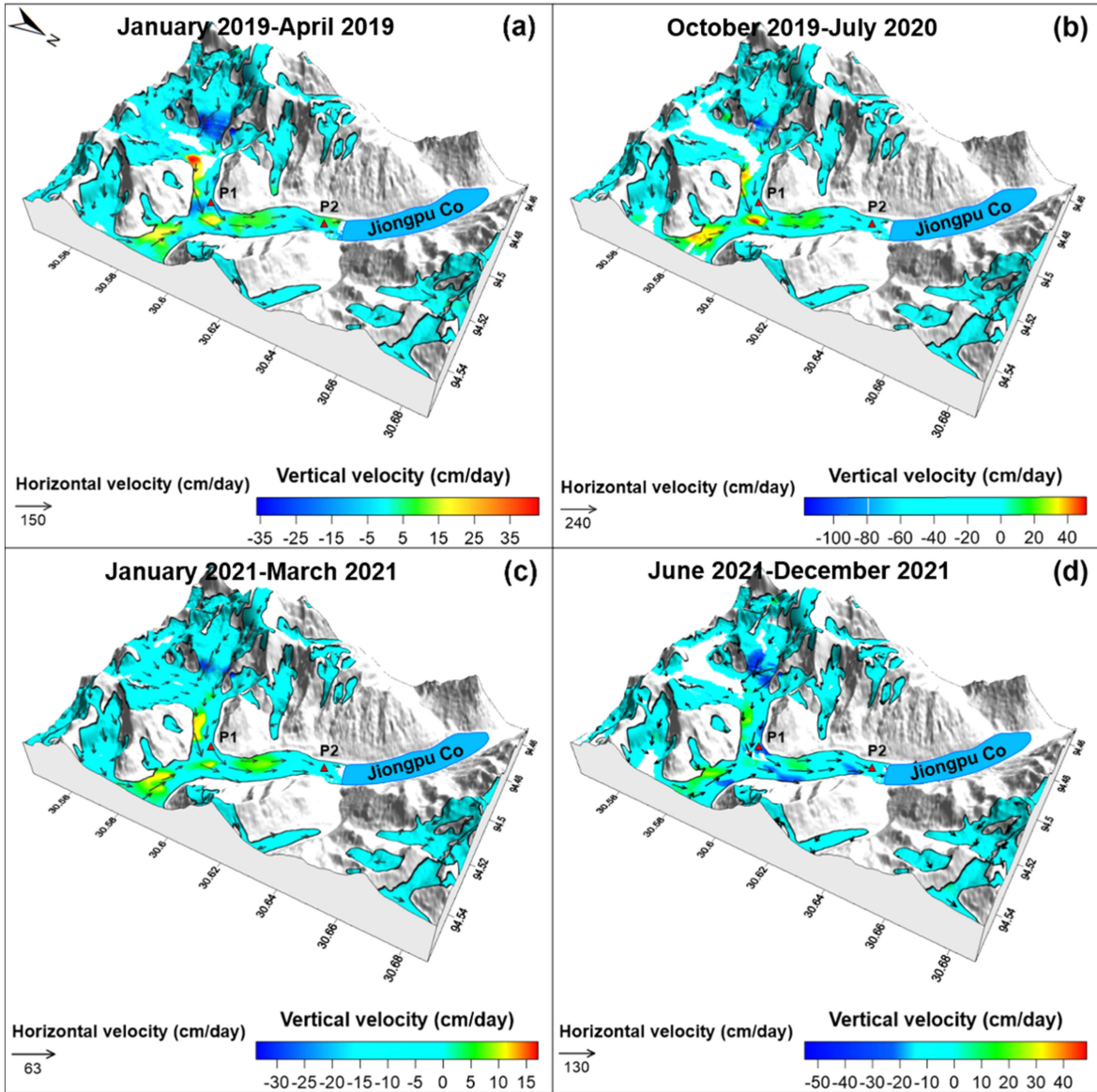


Fig. 3. Three-dimensional glacier flow velocities at four periods. (a)–(d) 3-D velocities between January 2019 and April 2019, October 2019 and July 2020, January 2021 and March 2021, June 2021 and December 2021, respectively. The same Sentinel-1 SAR dataset was used in [31].

data-scarce regions, where direct observations (e.g., ground-penetrating radar or borehole measurements) are typically unavailable. Prior studies have demonstrated that in such contexts, sensitivity analyses serve as effective tools for assessing the robustness and stability of glacier thickness estimates [1], [38], [39].

In our Monte Carlo framework, we introduced random perturbations to key input variables, including the rheological parameter, 3-D velocities, and slope. For each perturbed realization, the glacier thickness was reinverted, and this process was repeated for a large number of iterations. The ensemble of thickness enabled us to quantify uncertainty at each spatial location.

We calculated the standard deviation ( $\sigma$ ) and the coefficient of variation (CV) from the resulting ensemble to describe the spatial distribution of inversion uncertainty. These metrics are

defined as

$$\begin{cases} \sigma(x, y) = \sqrt{\frac{1}{N} \sum_{i=1}^N (H_i(x, y) - \bar{H}(x, y))^2} \\ cv(x, y) = \sigma(x, y) / \bar{H}(x, y) \end{cases} \quad (7)$$

where  $H_i(x, y)$  is the ice thickness at location  $(x, y)$  from the  $i$ th simulation,  $\bar{H}(x, y)$  is the ensemble mean thickness, and  $N$  is the total number of Monte Carlo simulations. The CV, defined as the ratio of the standard deviation (STD) to the mean thickness, provides a normalized measure of thickness uncertainty and is used here to indicate inversion stability.

In addition, to assess the consistency and robustness of our inversion results, we compared the thickness change rates between our results across multiple time periods and ICESat-2 observations. Multiperiod elevation differencing of land ice

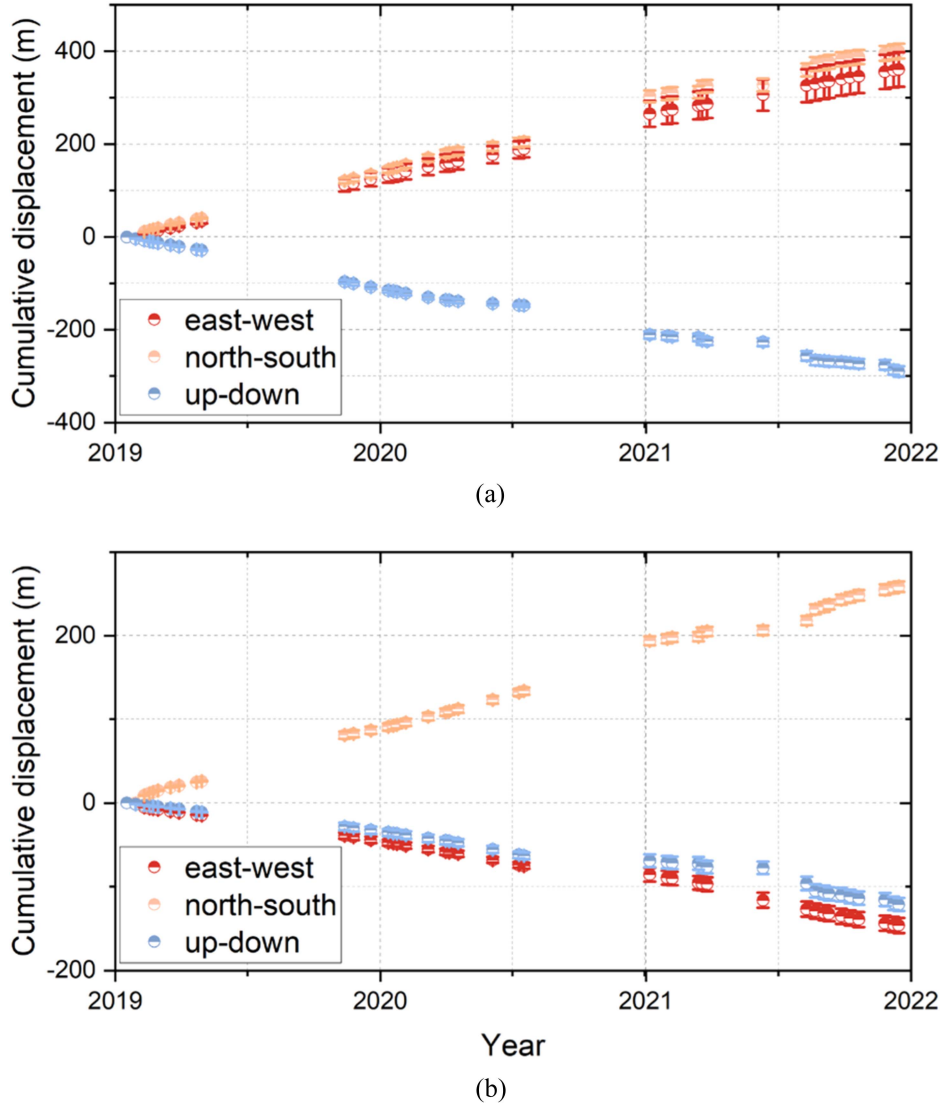


Fig. 4. Three-dimensional displacement time series of the Jiongpu glacier at (a) P1 and (b) P2 from 2019 to 2022. Error bars represent the STD of glacier displacement.

height using ATL06 products is an indispensable method to obtain the glacier thickness change.

#### IV. RESULTS

##### A. Glacier 3-D Velocities and Displacement Time Series

We derived the 3-D flow velocities of the Jiongpu glacier from January 2019 to December 2021 using the PO-MSBAS method, based on the same Sentinel-1 SAR dataset as in our previous publication [31]. Due to discontinuities in the descending Sentinel-1 SAR image, we separated the velocity results into four phases, as shown in Fig. 3. The maximum horizontal flow velocity from January 2019 to April 2019 (Period 1) reached 150 cm/day [see Fig. 3(a)]. The peak downward motion was observed at the summit of the western tributary, measuring 36 cm/day, while the maximum upward motion was 43 cm/day. Fig. 3(b) shows the 3-D velocities from October 2019 to July 2020 (Period 2). The highest horizontal velocity increased to

240 cm/day at the confluence of the western tributary and the main trunk. The maximum downward and upward velocities were 118 cm/day and 51 cm/day, respectively. Fig. 3(c) illustrates the 3-D glacier flow velocities from January 2021 to March 2021 (Period 3), with a maximum horizontal flow rate of 63 cm/day. The highest horizontal velocity was observed at the confluence of the western tributary and the main branch. The maximum downward motion occurred at the peak of the western tributary, measuring 34 cm/day, while the upward motion reached 17 cm/day along the main branch. The maximum horizontal velocity from June 2021 to December 2021 (Period 4) arrived at 130 cm/day, as shown in Fig. 3(d). The highest upward vertical velocity was 49 cm/day. Notably, during this period, the main branch exhibited a maximum downward velocity of 55 cm/day.

To capture the temporal evolution of motion, we extracted the time series of 3-D displacements at two selected points (see Fig. 4). As shown in Fig. 3, P1 is situated on the glacier's

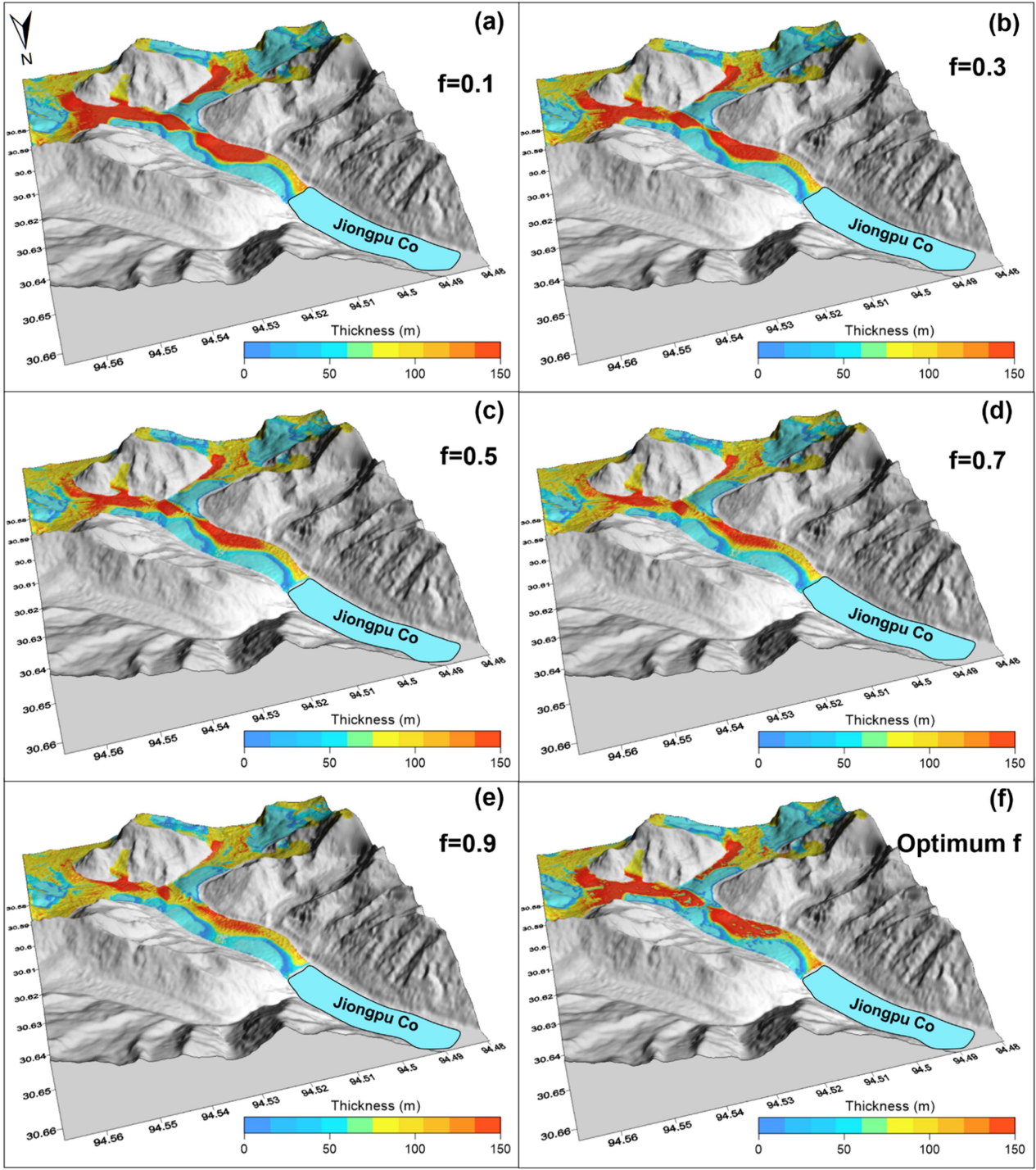


Fig. 5. Glacier thickness with varied rheological parameters. (a)–(e) Glacier thickness with rheological parameters ranging from 0.1, 0.3, 0.5, 0.7, 0.9, respectively. (f) Glacier thickness with the optimum rheological parameter, as shown in Fig. 6(d).

western tributary, while P2 is located near Jiongpu lake. The displacement time series from 2019 to 2022 was reconstructed by fitting temporal subsets and interpolating across gaps in the data [44]. We evaluated the uncertainties in the 3-D velocity fields by computing the STD within a  $3 \times 3$  pixel window centered on each point. This approach is widely used for uncertainty estimation in 3-D glacier velocity measurements [45].

P1 exhibited northward motion in the north-south direction, with a cumulative displacement of  $400 \pm 16$  m. In the eastward direction, the displacement was  $361 \pm 37$  m. The cumulative downward displacement reached  $291 \pm 11$  m in the vertical direction from 2019 to 2021. For P2, the cumulative displacements were  $259 \pm 7$  m in the north-south direction,  $146 \pm 9$  m in the east-west direction, and  $122 \pm 8$  m in the vertical direction. Both points exhibited consistent northward and downward

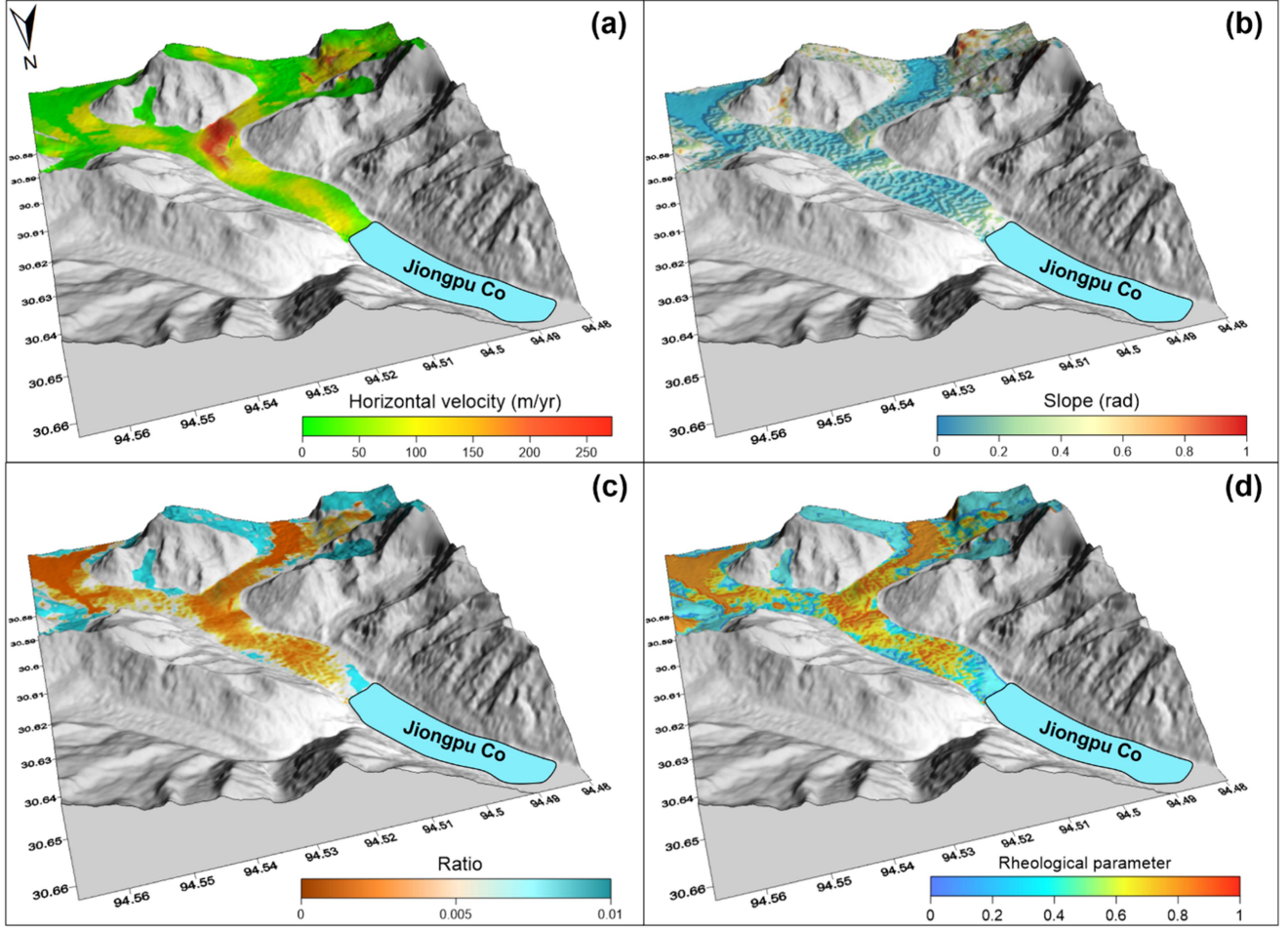


Fig. 6. Choice of rheological parameter. (a) Averaged horizontal velocity of the glacier (units: m/yr). (b) Slope of the glacier (units: radian). (c) Ratio of the slope and surface velocity. (d) Optimum rheological parameter. The visualization is generated from the same velocity dataset as in [31], but with a different spatial coverage and analytical context.

glacier motion. P1 moved eastward, while P2 moved westward, which aligns with the local topography. The glacier exhibited downward movement at both points, P1 and P2.

#### B. Glacier Thickness With Varied Rheological Parameters

We investigated the glacier thickness under a range of rheological parameters, from 0.1 to 0.9. Fig. 5 presents the spatial distribution of glacier thickness corresponding to different rheological parameters, including the optimal estimate. A larger rheological parameter yields a thinner glacier for the same 3-D velocity field, indicating an inverse relationship between the rheological parameter and estimated glacier thickness.

To obtain an optimized glacier thickness distribution, we further calibrated the rheological parameter using a spatially variable approach. Based on (6), we computed the ratio between the terrain slope and the averaged horizontal velocity to parameterize the rheological coefficient, as illustrated in Fig. 6. The visualization is based on the same velocity dataset as in our previous publication [31], but with a different spatial extent and analytical focus. Fig. 6(a) displays the averaged horizontal velocity, with a maximum velocity of 272 m/yr occurring at

the confluence of the western tributary and the main trunk. Fig. 6(b) shows that the calculated average slope angle over the glacier is approximately 10°. Fig. 6(c) shows the ratio between glacier surface slope and horizontal velocity. Fig. 6(d) shows the distribution of rheological parameter  $f$ . The applied rheological parameter mainly ranges from 0.4 to 0.9, consistent with conditions of temperate glaciers [10], [20], [38]. Rather than applying a single empirical rheological value across the glacier, we adopted a spatially variable approach to update the rheological parameter field. This allowed for the derivation of an optimized glacier thickness distribution, as shown in Fig. 5(f).

## V. DISCUSSIONS

### A. Sensitivity Analysis of Glacier Thickness to Rheological Parameters

To assess the sensitivity of glacier thickness inversion to variations in the rheological parameter, we conducted Monte Carlo simulations by perturbing the flow factor  $f$  across a range from 0 to 1. As shown in Fig. 7(a), the mean glacier thickness decreases with higher values of  $f$ . The STD of glacier thickness [see Fig. 7(b)] increases with higher  $f$ . The STD reaches over

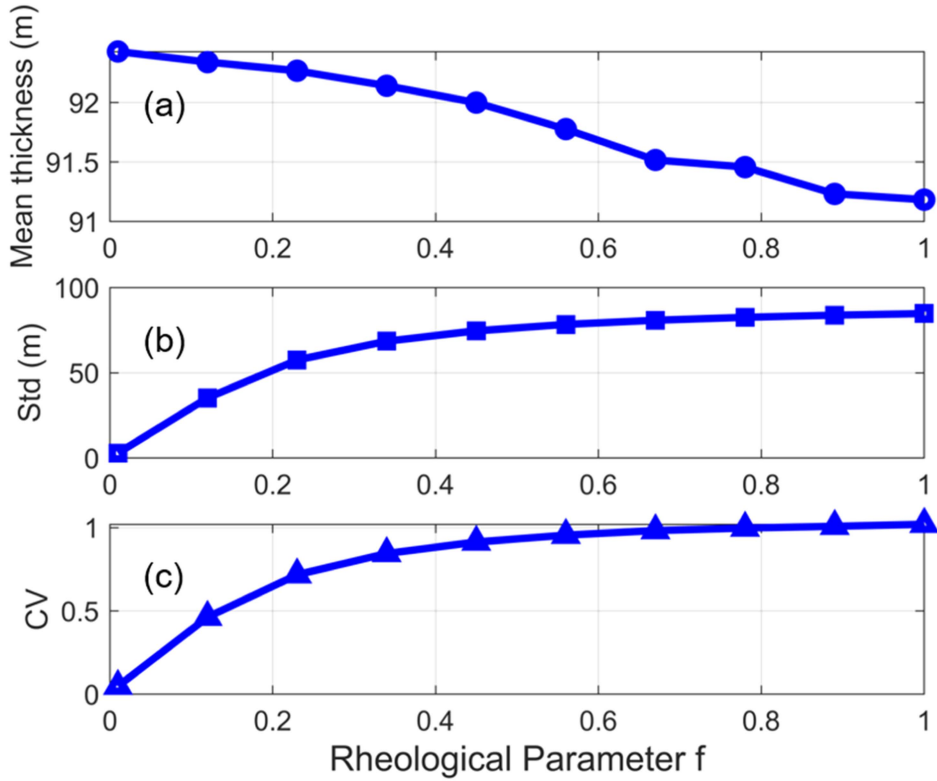


Fig. 7. Sensitivity of glacier thickness to rheological parameters. (a) Glacier mean thickness, (b) STD, and (c) CV under different rheology parameters.

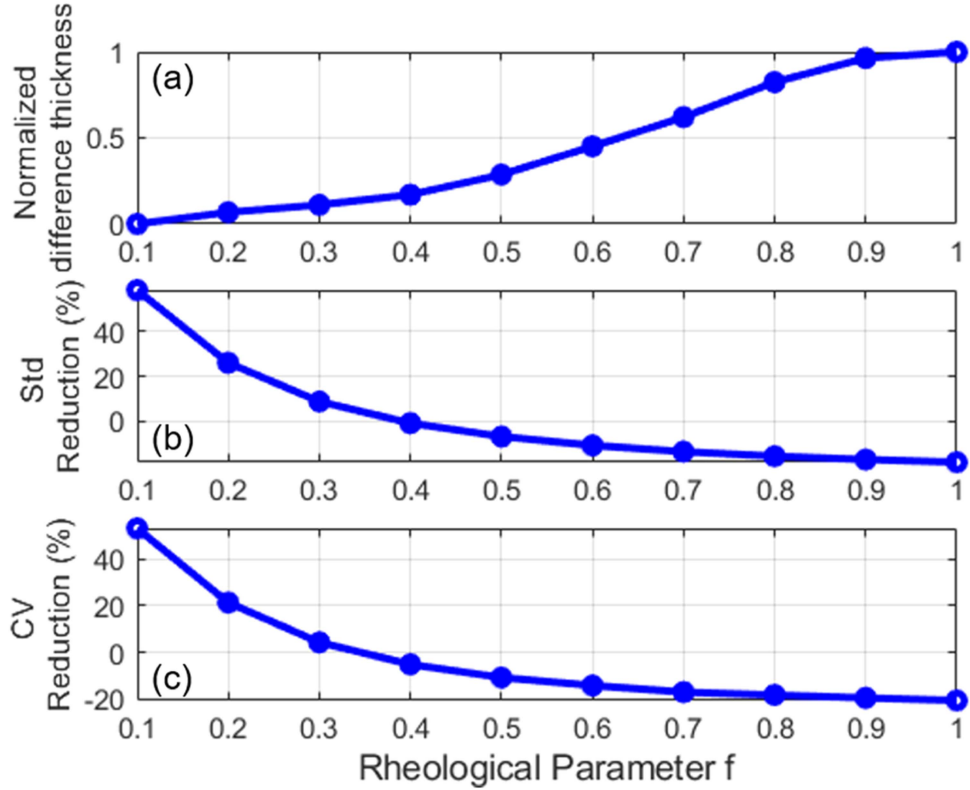


Fig. 8. Difference between optimized and fixed rheological parameters ranging from 0 to 1. Difference in (a) normalized thickness, (b) STD, and (c) CV.

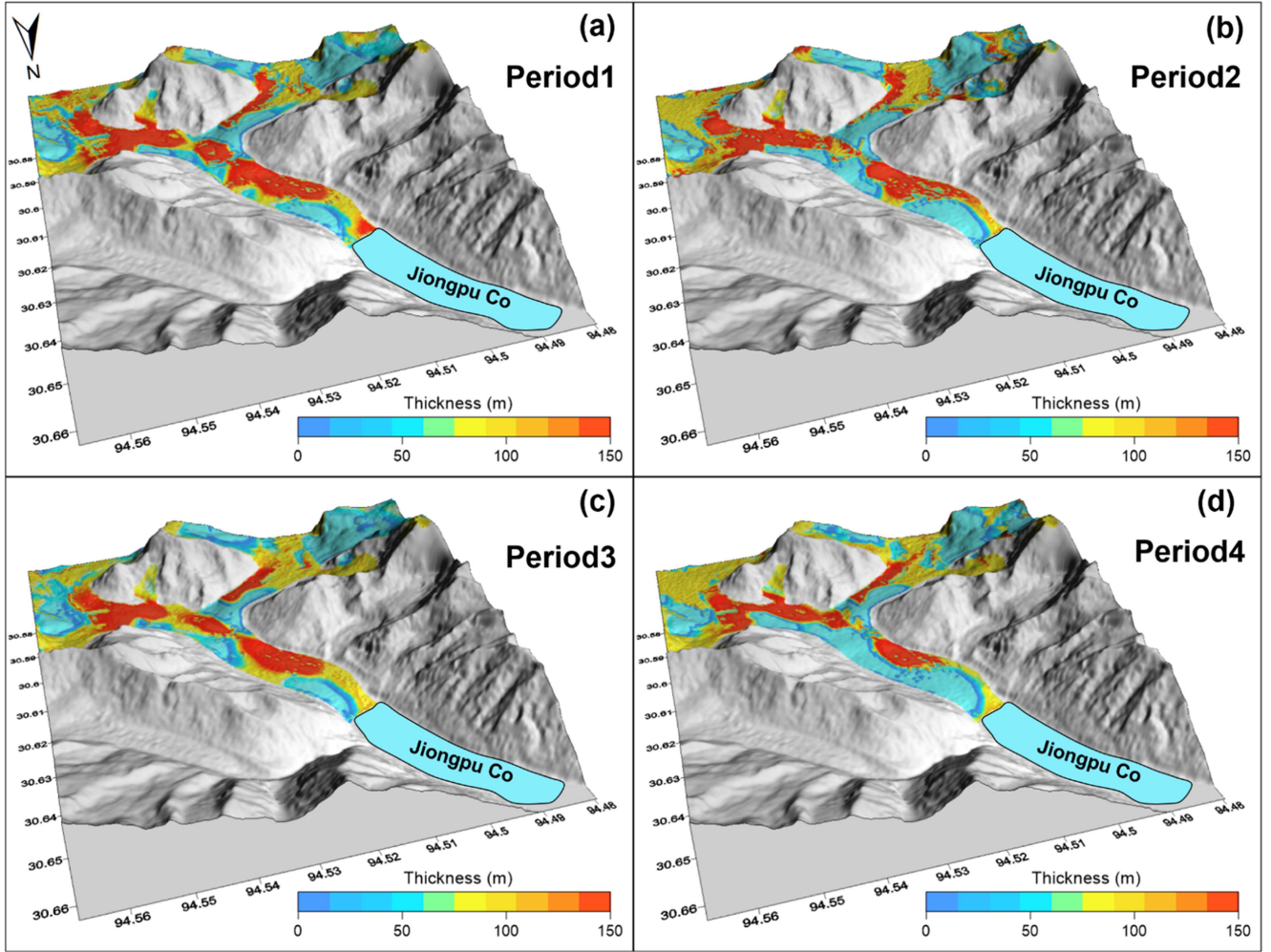


Fig. 9. Glacier thickness results using time-specific 3-D velocities in four periods. (a)–(d) Glacier thickness results from January 2019 to April 2019, October 2019 to July 2020, January 2021 to March 2021, June 2021 to December 2021, respectively.

80 m when  $f > 0.6$ . The CV of glacier thickness is shown in Fig. 7(c). When  $f$  is greater than 0.6, the CV approaches 1, indicating that the thickness results are gradually unstable. These results highlight that glacier thickness inversion is highly sensitive to the selection of rheological parameters, emphasizing the necessity of optimizing the rheological parameters.

To evaluate the benefits of this optimization, we compared the thickness in mean value, STD, and CV between models using our optimum  $f$  and fixed  $f$  values (ranging from 0 to 1).

Fig. 8(a) shows the difference in the normalization mean thickness between optimum and fixed rheological parameters. As  $f$  increases, the difference between the optimum and fixed values  $f$  gradually increases. Fig. 8(b)–(c) indicates our optimized rheological parameter achieves reductions in uncertainty with  $f$  0.4, including STD and CV. The maximum reductions reach 18.4% and 20.4%, respectively. In the lower  $f$  range (0.1–0.2), minor increases in uncertainty are observed, which may be attributed to the inherently weak sensitivity of the thickness result, as shown in Fig. 7. In addition, our optimum rheological parameter of the Jiongpu glacier is mainly greater than 0.4. Moreover, it is worth noting that rheological parameters

close to 0.1 are physically unrealistic for temperate glaciers in southeastern Tibet, where ice is typically warm-based and deformable [17], [40].

These findings confirm that the effectiveness of employing a spatially adaptive rheological parameter, derived from surface slope and horizontal velocity. This adaptive approach contributes to reducing inversion uncertainty, especially with high rheological parameters.

#### B. Sensitivity Analysis of Glacier Thickness to Time-Variable Ice Velocity

The four distinct 3-D velocity periods shown in Fig. 3 were derived from SAR datasets spanning from 2019 to 2021. They may significantly influence the resulting glacier thickness distribution. To assess the impact of glacier flow velocity on glacier thickness, we conducted a sensitivity analysis in which glacier thickness was inverted independently for each period using the corresponding 3-D glacier velocities.

Fig. 9 presents the resulting glacier thickness maps for each period, highlighting spatiotemporal variations attributable to

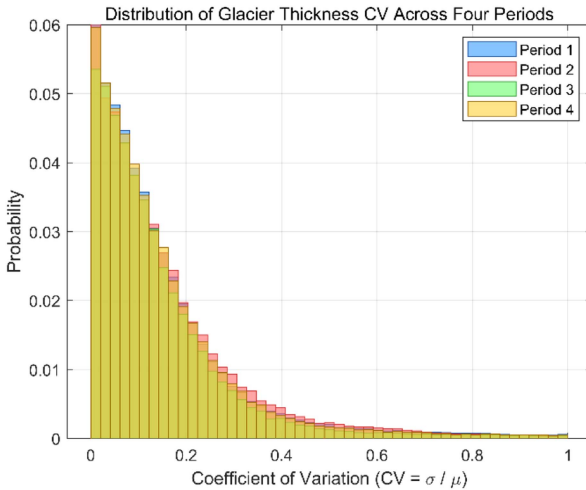


Fig. 10. Spatial distribution of the CV of glacier thickness across four velocity periods.

TABLE I  
QUANTITATIVE IMPACT OF INCORPORATING VERTICAL VELOCITY ON GLACIER THICKNESS INVERSION

Period	Mean CV without vertical velocity	Mean CV with vertical velocity	CV reduction (%)
1	1.68	1.03	38.70
2	1.70	1.04	38.82
3	1.78	1.03	42.13
4	1.64	1.04	36.59

For each time period, we report the mean CV with and without vertical velocity, and the percentage reduction in CV.

changes in 3-D velocity. While the overall thickness patterns remain consistent, especially in the accumulation zone and the central trunk, noticeable local differences are observed near the glacier terminus and in steep-sloped regions.

To quantify this temporal sensitivity, we computed the CV of glacier thickness across the four periods. As shown in Fig. 10, the distribution of CV values reveals overall variability in the sensitivity of glacier thickness to temporal velocity changes. Most areas exhibit low-to-moderate sensitivity ( $CV < 0.2$ ), reflecting stable inversion results despite changes in ice velocity. A smaller portion shows higher sensitivity ( $CV > 0.3$ ). These dynamically active regions are more responsive to short-term changes in glacier motion due to enhanced basal sliding and strain-rate variations, resulting in greater temporal variability in thickness inversion [46].

Our inversion thickness method provides the feasibility of obtaining the thickness distribution under various 3-D velocity fields.

To quantitatively assess the effect of incorporating vertical velocity on the accuracy and stability of glacier thickness inversion, we conducted a set of Monte Carlo simulations under two scenarios: 1) using only the horizontal surface velocity, and 2) incorporating both horizontal and vertical velocity components.

For each of the four time periods, we calculated the CV of the inverted thickness results. As summarized in Table I, the

TABLE II  
MEAN STD OF GLACIER THICKNESS (IN M) UNDER DIFFERENT SLOPE PERTURBATION SCENARIOS FOR EACH OBSERVATION PERIOD

Period	$\pm 0.3^\circ$ slope error	$\pm 1.0^\circ$ slope error	$\pm 2.0^\circ$ slope error
1	2.38 m	4.50 m	6.08 m
2	2.39 m	4.50 m	6.07 m
3	1.18 m	2.45 m	3.71 m
4	2.66 m	4.44 m	5.76 m

inclusion of vertical velocity led to a substantial reduction in the CV across all periods, ranging from 36.59% to 42.13%. For example, during Period 3, the mean CV decreased from 1.78 (without vertical velocity) to 1.03 (with vertical velocity), corresponding to a 42.13% reduction. This highlights the significant contribution of vertical motion in enhancing the accuracy and stability of glacier thickness inversion.

### C. Sensitivity Analysis of Glacier Thickness to Slope Change

To evaluate the sensitivity of glacier thickness to uncertainties in slope estimation, we conducted a series of controlled perturbation experiments on the DEM-derived slope. It is essential to assess how elevation errors may propagate through to the final thickness results.

Artificial slope perturbations were introduced at three levels:  $\pm 0.3^\circ$ ,  $\pm 1.0^\circ$ , and  $\pm 2.0^\circ$ . For each perturbation level, we performed Monte Carlo simulations using the modified slope fields while keeping all other parameters constant. The STD of the resulting glacier thickness was computed to quantify the impact of these slope changes.

Fig. 11 shows histograms of the thickness STD under the three levels of slope perturbation across four time periods. The distributions exhibit that the majority of the values are concentrated below 10 m. The results highlight that small slope errors can introduce variability in ice thickness estimates.

Table II summarizes the average STD of ice thickness for each period and perturbation level. A slope error of  $\pm 0.3^\circ$  results in average uncertainties ranging from 1.18 to 2.66 m, depending on the observation period. In contrast, a slope perturbation of  $\pm 2.0^\circ$  leads to greater uncertainty, with mean STD values reaching up to 6.08 m.

These results indicate that slope uncertainty can introduce variability in thickness inversion. When the average glacier thickness in our study ranges between 60 and 120 m, the relative uncertainty ranges from 3.1% to 10.1%.

### D. Consistency Evaluation Using Multitemporal Thickness Change Rates and ICESat-2 Datasets

To further evaluate the consistency of our inversion framework, we reconstructed glacier thickness at four distinct time periods, as shown in Fig. 9. Based on these reconstructions, we calculated thickness change rates ( $dh/dt$ ) over three time intervals.

As illustrated in Fig. 12, panel (a) shows the histograms of glacier thickness change rates ( $dh/dt$ ) for three time periods,

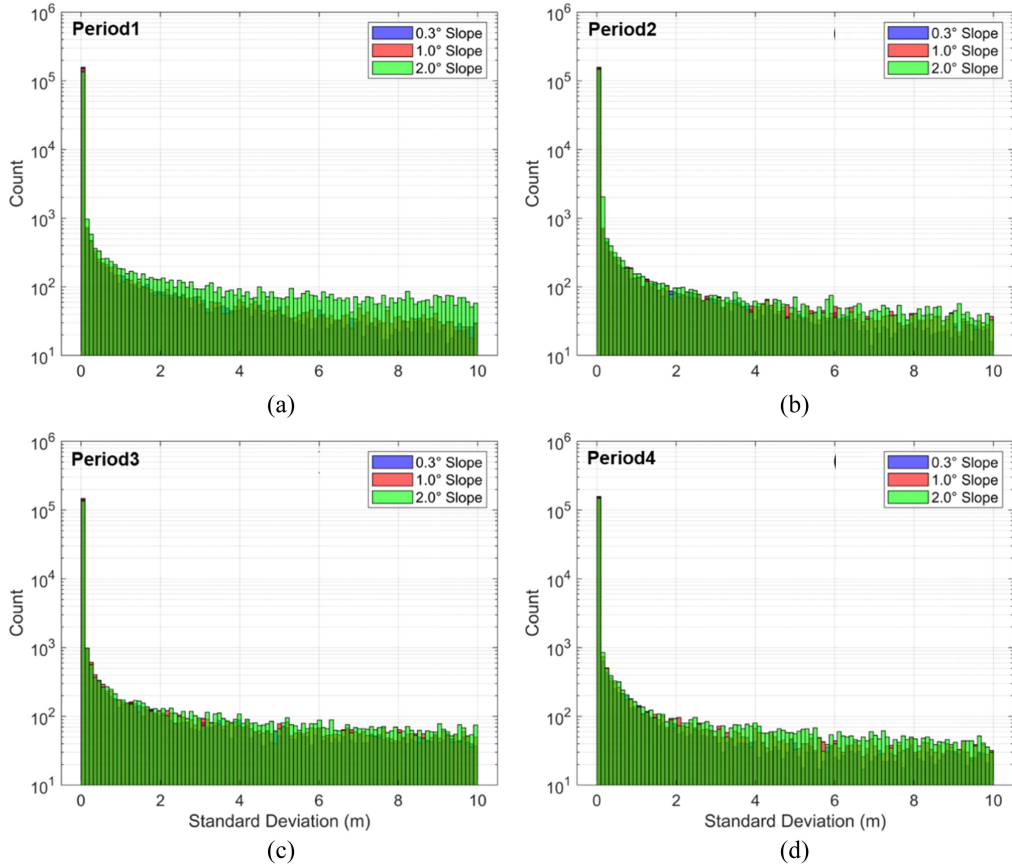


Fig. 11. Histograms of thickness STD to slope perturbation in four periods under artificial slope errors of  $\pm 0.3^\circ$ ,  $\pm 1.0^\circ$ , and  $\pm 2.0^\circ$ . (a)–(d) Mean STD of ice thickness from January 2019 to April 2019, October 2019 to July 2020, January 2021 to March 2021, June 2021 to December 2021, respectively.

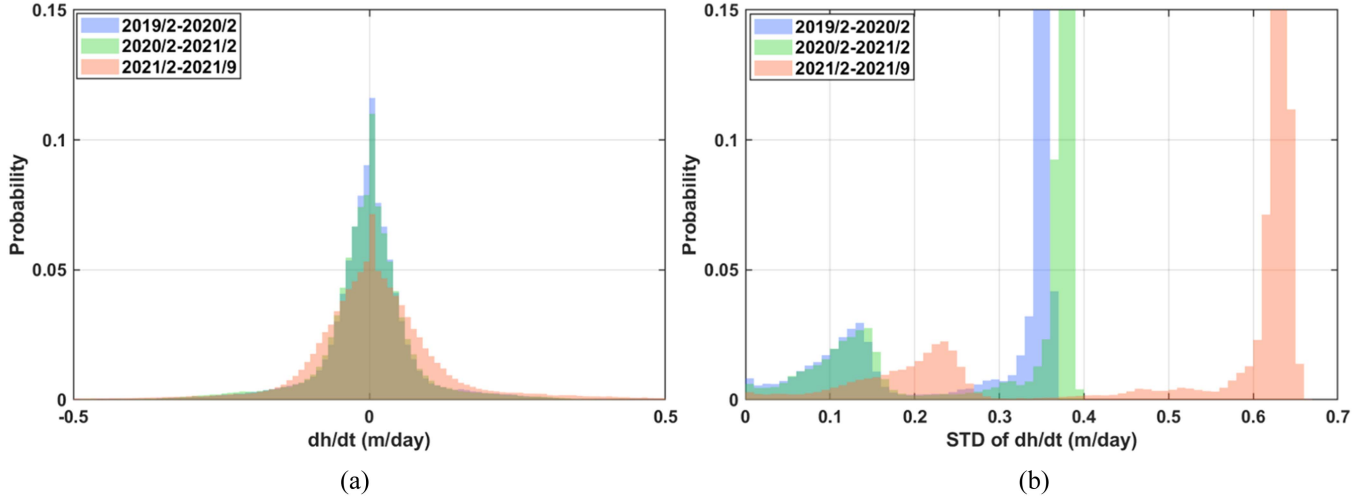


Fig. 12. Thickness change rates ( $dh/dt$ ) and their associated uncertainties over three time intervals of the Jiongpu glacier. (a) Histograms of  $dh/dt$  from February 2019 to February 2020 ( $\sim 12$  months), February 2020 to February 2021 ( $\sim 12$  months), and February 2021 to September 2021 (only  $\sim 7$  months). (b) STD of  $dh/dt$  during three different periods.

while panel (b) displays the corresponding uncertainties, expressed as the STD of  $dh/dt$ . The  $dh/dt$  values for most pixels generally range between  $-0.5$  and  $0.5$  m/day. The mean STDs of  $dh/dt$  for the three periods are  $0.29$ ,  $0.31$ , and  $0.52$  m/day, respectively. Notably, the highest STD is observed in the third period (February 2021 to September 2021), which can be attributed to

the shorter time interval and the inclusion of ablation-intensive seasons.

To evaluate the consistency of thickness changes between the ICESat-2 measurements and our model-based estimates, we compared the thickness change rates derived from ICESat-2 measurements with our results over different time periods.

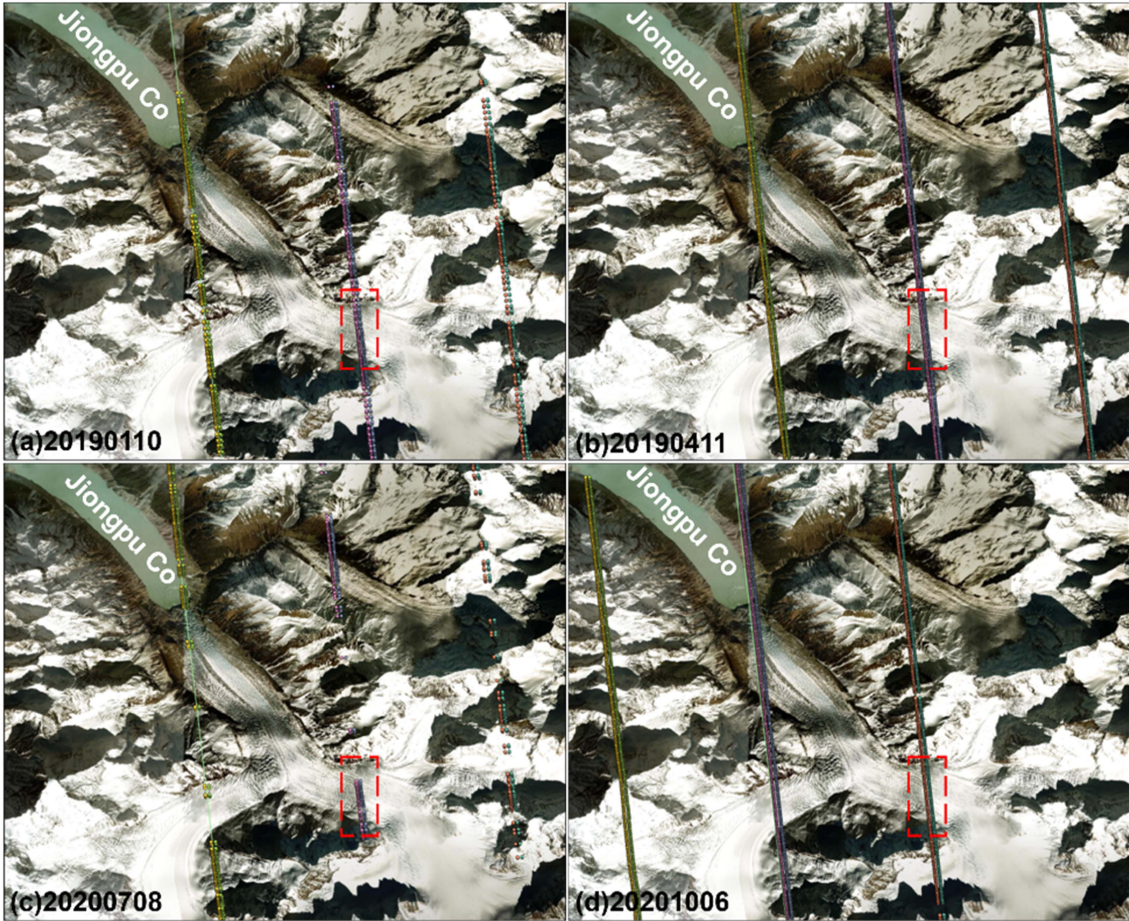


Fig. 13. Footprints of the six ICESat-2 ATL06 beams on the glacier surface from 2019 to 2020 (dates: yyyyymmdd). The background images are Google Earth maps.

Fig. 13 shows the footprints of six ATL06 laser beams on the glacier surface from January 2019 to October 2020. We observed that the distribution of the ICESat-2 laser beams varied at different times within the same orbit. The strong photons from the second-right, second-left, third-left, and third-left laser beams, observed on 10 January 2019, 11 April 2019, 8 July 2020, and 6 October 2020, were extracted to illustrate the elevation changes in the common area of the Jiongpu glacier. The thickness changes observed by ICESat-2 along glacier transects were obtained from elevation differences from January 2019 to October 2020.

Fig. 14(a) illustrates the thickness change along a common transect. Meanwhile, our thickness changes exhibit spatial variability due to varying time spans. The trends from February 2019 to February 2020, February 2020 to February 2021, are largely consistent with ICESat-2 observations. From February 2021 to September 2021, an accelerated thinning trend was clearly observed 2021. Fig. 14(b) presents the correlation matrix, showing a strong positive correlation between the ICESat-2 measurements and the period 1–2 estimates ( $R = 0.91$ ), a moderate correlation between period 2–3 ( $R = 0.68$ ), and a weaker correlation between period 3–4 ( $R = 0.38$ ). The decreasing correlation values can be attributed to the varying time between ICESat-2 measurements and each period of our thickness results.

It should be noted that the comparison with ICESat-2 elevation change does not serve as a direct validation of absolute ice thickness. Such indirect consistency checks are especially valuable in glacier regions where direct thickness measurements are unavailable.

By ensuring internal consistency among model outputs and external agreement with ICESat-2 observations, this approach provides a reliable framework for evaluating glacier dynamics, especially in regions lacking dense ground-based measurements.

#### E. Limitations and Future Directions

While the proposed method demonstrates promising performance on the studied glacier, its applicability to other glacier environments should be considered with respect to both terrain conditions and data availability. A primary limitation arises from layover and shadow effects inherent to SAR imaging, which are particularly severe in steep or rugged terrain and can restrict surface visibility. Because the reconstruction of 3-D surface velocity requires both ascending and descending SAR acquisitions, reduced visibility in either orbit may lead to spatial gaps or increase uncertainties in the velocity fields. In contrast, glaciers situated in open valleys or on moderately sloped terrain experience fewer visibility issues, making the method especially

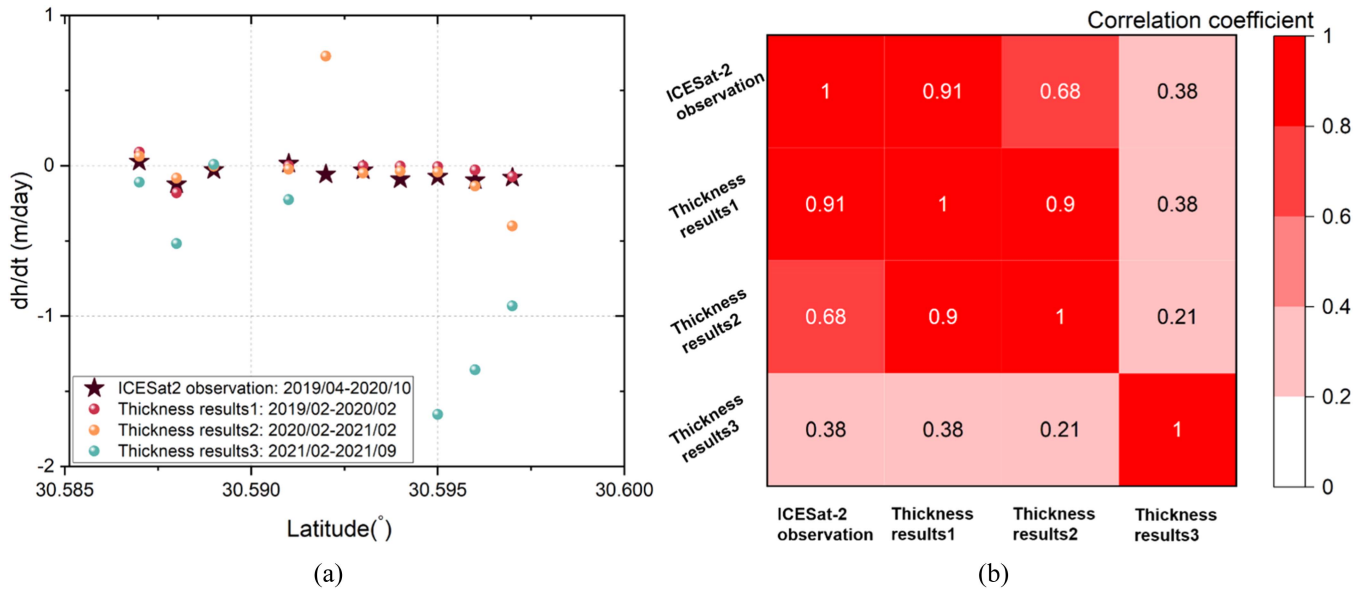


Fig. 14. Comparison of thickness change rates ( $dh/dt$ ) derived from multiperiod thickness and ICESat-2 observations. (a) Thickness change rates along a transect derived from ICESat-2 datasets and our modeled results. (b) Correlation matrix showing the Pearson correlation coefficients between ICESat-2-derived  $dh/dt$  and the modeled  $dh/dt$  from the three period.

effective in such settings. Under these favorable conditions, with high-quality ascending and descending acquisitions, the method can provide robust and spatially continuous 3-D velocity reconstructions.

In addition to terrain, the broader applicability of the framework is influenced by the availability and quality of multisource datasets. The inversion workflow requires ascending and descending SAR imagery, DEMs, and glacier-wide mass balance estimates. These datasets are not always uniformly accessible across different regions, and in data-scarce environments, the method may need to rely more heavily on prior assumptions or regularization strategies to stabilize the inversion [35], [36]. Moreover, glaciers covered by thick debris pose further challenges, as the insulating effect of debris alters flow dynamics and thickness distribution, potentially reducing the accuracy of velocity–thickness inversion [47]. These conditions highlight the importance of tailoring the approach to glacier-specific characteristics.

Nevertheless, the method remains well-suited for applications in regions with favorable SAR acquisition geometries and sufficient ancillary data. For glaciers located in narrow valleys or surrounded by steep headwalls, complementary observations such as optical stereo imagery or auxiliary topographic masks could help mitigate visibility limitations and strengthen inversion reliability. Looking ahead, enhancing the framework with advanced remote sensing technologies and machine learning techniques offers a promising avenue to improve robustness under suboptimal conditions and extend applicability to a wider variety of glacier types. Such developments would further strengthen the generalizability of the approach and its contribution to glacier monitoring in diverse glaciological settings.

In summary, the method is particularly applicable to

- 1) valley glaciers with moderate slopes where SAR layover and shadow are minimized,

- 2) debris-free or thinly debris-covered glaciers where flow dynamics can be well captured, and
- 3) regions where both ascending/descending SAR acquisitions and reliable DEMs are available.

Conversely, the applicability is more limited for steep headwall glaciers, heavily debris-covered glaciers, or data-scarce regions. This highlights that, under favorable geometric and data conditions, the proposed framework can be generalized to a broad range of glacier types, demonstrating its robustness and transferability.

## VI. CONCLUSION

This study proposes a remote sensing-based framework for estimating glacier thickness by leveraging 3-D surface velocities derived from multitrack SAR imagery. Using the PO-MSBAS technique, we reconstructed displacement time series and 3-D velocity fields of the Jiongpu glacier from 2019 to 2022. Glacier thickness was inverted through a Monte Carlo-based approach by solving the mass conservation equation, incorporating spatially adaptive rheological parameters determined from surface slope and horizontal velocity.

We conducted a sensitivity analysis to evaluate the impact of rheological parameters, time-variable 3-D velocities, and slope changes on glacier thickness inversion. Results show that employing a spatially adaptive rheological parameter significantly reduces inversion uncertainty. Incorporating vertical velocity enhances the thickness accuracy, with uncertainty reduction of 42.1%. Furthermore, consistency evaluation by comparing our multitemporal thickness change estimates with ICESat-2 observations confirmed the robustness of the inversion results in the absence of in-situ validation data.

By minimizing the dependence on in-situ measurements and detailed physical parameters, our method provides an efficient

approach for estimating glacier thickness variations across space and time, particularly in remote mountainous regions. It holds potential for application to mountain glaciers across High Mountain Asia, supporting monitoring of glacier evolution under ongoing climate change.

#### ACKNOWLEDGMENT

The authors would like to thank the Alaska Satellite Facility (ASF) for providing Sentinel-1 SAR datasets and ALOS PALSAR DEM (<https://vertex.daac.asf.alaska.edu/#>), CGIAR-CSI for providing C-band SRTM DEMs (<http://srtm.csi.cgiar.org/>), and ICESat-2 Mission for providing ICESat-2 ATL06 datasets (<https://icesat-2.gsfc.nasa.gov/icesat-2-data>).

#### REFERENCES

- [1] D. Farinotti et al., "How accurate are estimates of glacier ice thickness? results from ITMIX, the ice thickness models intercomparison eXperiment," *Cryosphere*, vol. 11, no. 2, pp. 949–970, Nov. 2017, doi: [10.5194/tc-2016-250](https://doi.org/10.5194/tc-2016-250), 2016.
- [2] D. Farinotti et al., "Results from the ice thickness models intercomparison eXperiment phase 2 (ITMIX2)," *Front. Earth Sci.*, vol. 8, Jan. 2021, Art. no. 571923, doi: [10.3389/feart.2020.571923](https://doi.org/10.3389/feart.2020.571923).
- [3] R. Hock and M. Huss, "Glaciers and climate change," in *Climate Change*. Amsterdam, The Netherlands: Elsevier, pp. 157–176, Jan. 2021, doi: [10.1016/B978-0-12-821575-3.00009-8](https://doi.org/10.1016/B978-0-12-821575-3.00009-8).
- [4] S. K. Allen et al., "Potentially dangerous glacial lakes across the Tibetan Plateau revealed using a large-scale automated assessment approach," *Sci. Bull.*, vol. 64, no. 7, pp. 435–445, Apr. 2019, doi: [10.1016/j.scib.2019.03.011](https://doi.org/10.1016/j.scib.2019.03.011).
- [5] L. Yang et al., "Glacial lake outburst flood monitoring and modeling through integrating multiple remote sensing methods and HEC-RAS," *Remote Sens.*, vol. 15, no. 22, Nov. 2023, Art. no. 5327, doi: [10.3390/rs15225327](https://doi.org/10.3390/rs15225327).
- [6] T. Chinn et al., "Annual ice volume changes 1976–2008 for the New Zealand Southern Alps," *Glob. Planet. Change*, vol. 92, pp. 105–118, Jul. 2012, doi: [10.1016/j.gloplacha.2012.04.002](https://doi.org/10.1016/j.gloplacha.2012.04.002).
- [7] R. Hugonet et al., "Accelerated global glacier mass loss in the early twenty-first century," *Nature*, vol. 592, no. 7856, pp. 726–731, Apr. 2021, doi: [10.1038/s41586-021-03436-z](https://doi.org/10.1038/s41586-021-03436-z).
- [8] M. Zemp et al., "Global glacier mass changes and their contributions to sea-level rise from 1961 to 2016," *Nature*, vol. 568, no. 7752, pp. 382–386, Apr. 2019, doi: [10.1038/s41586-019-1071-0](https://doi.org/10.1038/s41586-019-1071-0).
- [9] E. Welty et al., "Worldwide version-controlled database of glacier thickness observations," *Earth Syst. Sci. Data Discuss.*, vol. 12, no. 4, pp. 3039–3055, May 2020, doi: [10.5194/essd-12-3039-2020](https://doi.org/10.5194/essd-12-3039-2020).
- [10] M. Morlighem et al., "A mass conservation approach for mapping glacier ice thickness," *Geophys. Res. Lett.*, vol. 38, no. 19, Oct. 2011, Art. no. L19503, doi: [10.1029/2011GL048659](https://doi.org/10.1029/2011GL048659).
- [11] J. Chen and A. Ohmura, "Estimation of alpine glacier water resources and their change since the 1870s," *IAHS Publ.*, vol. 193, pp. 127–135, Aug. 1990.
- [12] D. B. Bahr, M. F. Meier, and S. D. Peckham, "The physical basis of glacier volume-area scaling," *J. Geophys. Res., Solid Earth*, vol. 102, no. B9, pp. 20355–20362, Sep. 1997, doi: [10.1029/97JB01696](https://doi.org/10.1029/97JB01696).
- [13] A. Grinsted, "An estimate of global glacier volume," *Cryosphere*, vol. 7, no. 1, pp. 141–151, Jan. 2013, doi: [10.5194/tc-7-141-2013](https://doi.org/10.5194/tc-7-141-2013).
- [14] C. F. Brædstrup et al., "Basal shear stress under alpine glaciers: Insights from experiments using the iSOSIA and Elmer/ice models," *Earth Surf. Dyn.*, vol. 4, no. 1, pp. 159–174, Feb. 2016, doi: [10.5194/esurf-4-159-2016](https://doi.org/10.5194/esurf-4-159-2016).
- [15] M. Huss and D. Farinotti, "A high-resolution bedrock map for the Antarctic Peninsula," *Cryosphere*, vol. 8, no. 4, pp. 1261–1273, Jul. 2014, doi: [10.5194/tc-8-1261-2014](https://doi.org/10.5194/tc-8-1261-2014).
- [16] D. J. Brinkerhoff and J. V. Johnson, "Dynamics of thermally induced ice streams simulated with a higher-order flow model," *J. Geophys. Res., Earth Surf.*, vol. 120, no. 9, pp. 1743–1770, Sep. 2015, doi: [10.1002/2015JF003499](https://doi.org/10.1002/2015JF003499).
- [17] D. Farinotti, H. Corr, and G. H. Gudmundsson, "The ice thickness distribution of Flask Glacier, Antarctic Peninsula, determined by combining radio-echo soundings, surface velocity data and flow modelling," *Ann. Glaciol.*, vol. 54, no. 63, pp. 18–24, Jan. 2013, doi: [10.3189/2013AoG63A603](https://doi.org/10.3189/2013AoG63A603).
- [18] G. K. C. Clarke et al., "Neural networks applied to estimating subglacial topography and glacier volume," *J. Climate*, vol. 22, no. 8, pp. 2146–2160, Apr. 2009, doi: [10.1175/2008JCLI2572.1](https://doi.org/10.1175/2008JCLI2572.1).
- [19] M. A. Haq, K. Jain, and K. P. R. Menon, "Modelling of Gangotri glacier thickness and volume using an artificial neural network," *Int. J. Remote Sens.*, vol. 35, no. 16, pp. 6035–6042, Aug. 2014, doi: [10.1080/01431161.2014.943322](https://doi.org/10.1080/01431161.2014.943322).
- [20] R. Millan et al., "Ice velocity and thickness of the world's glaciers," *Nat. Geosci.*, vol. 15, no. 2, pp. 124–129, Feb. 2022, doi: [10.1038/s41561-021-00885-z](https://doi.org/10.1038/s41561-021-00885-z).
- [21] S. Samsonov, K. Tiampo, and R. Cassotto, "SAR-derived flow velocity and its link to glacier surface elevation change and mass balance," *Remote Sens. Environ.*, vol. 258, Jun. 2021, Art. no. 112343, doi: [10.1016/j.rse.2021.112343](https://doi.org/10.1016/j.rse.2021.112343).
- [22] T. Strozzi, A. Luckman, T. Murray, U. Wegmüller, and C. L. Werner, "Glacier motion estimation using SAR offset-tracking procedures," *IEEE Trans. Geosci. Remote Sens.*, vol. 40, no. 11, pp. 2384–2391, Nov. 2002, doi: [10.1109/TGRS.2002.805079](https://doi.org/10.1109/TGRS.2002.805079).
- [23] L. Yang et al., "Analyzing the triggering factors of glacial lake outburst floods with SAR and optical images: A case study in Jinweng Co, Tibet, China," *Landslides*, vol. 19, no. 4, pp. 855–864, Apr. 2022, doi: [10.1007/s10346-021-01831-1](https://doi.org/10.1007/s10346-021-01831-1).
- [24] T. Strozzi et al., "Estimation of Arctic glacier motion with satellite L-band SAR data," *Remote Sens. Environ.*, vol. 112, no. 3, pp. 636–645, Mar. 2008, doi: [10.1016/j.rse.2007.06.007](https://doi.org/10.1016/j.rse.2007.06.007).
- [25] J. Li et al., "Deriving a time series of 3D glacier motion to investigate interactions of a large mountain glacial system with its glacial lake: Use of synthetic aperture radar pixel offset-small baseline subset technique," *J. Hydrol.*, vol. 559, pp. 596–608, Apr. 2018, doi: [10.1016/j.jhydrol.2018.02.067](https://doi.org/10.1016/j.jhydrol.2018.02.067).
- [26] L. Yang et al., "Three-dimensional time series movement of the Cuolangma glaciers, southern Tibet with Sentinel-1 imagery," *Remote Sens.*, vol. 12, no. 20, Oct. 2020, Art. no. 3466, doi: [10.3390/rs12203466](https://doi.org/10.3390/rs12203466).
- [27] G. Zhang et al., "Underestimated mass loss from lake-terminating glaciers in the greater Himalaya," *Nat. Geosci.*, vol. 16, no. 4, pp. 333–338, Apr. 2023, doi: [10.1038/s41561-023-01150-1](https://doi.org/10.1038/s41561-023-01150-1).
- [28] T. Peng et al., "Risk assessment of a glacial lake with abruptly slowing expansion, Jiongpu, Southeastern Tibet," *Geomorphology*, vol. 468, Jan. 2025, Art. no. 109471, doi: [10.1016/j.geomorph.2024.109471](https://doi.org/10.1016/j.geomorph.2024.109471).
- [29] W. W. Immerzeel, L. P. H. Van Beek, and M. F. P. Bierkens, "Climate change will affect the Asian water towers," *Science*, vol. 328, no. 5984, pp. 1382–1385, Jul. 2010, doi: [10.1126/science.1183188](https://doi.org/10.1126/science.1183188).
- [30] W. Yang et al., "Mass balance of a maritime glacier on the southeast Tibetan Plateau and its climatic sensitivity," *J. Geophys. Res., Atmos.*, vol. 118, no. 17, pp. 9579–9594, Dec. 2013.
- [31] L. Yang et al., "Studying mass movement sources and potential glacial lake outburst flood at Jiongpu Co, southeastern Tibet, using multiple remote sensing methods and HEC-RAS model," *J. Geophys. Res., Earth Surf.*, vol. 130, no. 7, pp. 1–28, Jul. 2025, doi: [10.1029/2024JF008067](https://doi.org/10.1029/2024JF008067).
- [32] D. Li et al., "An ice loss evaluation of lake-terminating glaciers based on lake bathymetry—A case study of the Jiongpu Glacier," *Remote Sens.*, vol. 16, no. 16, Aug. 2024, Art. no. 3027, doi: [10.3390/rs16163027](https://doi.org/10.3390/rs16163027).
- [33] S. V. Samsonov et al., "Rapidly accelerating subsidence in the greater Vancouver region from two decades of ERS-ENVISAT-RADARSAT-2 InSAR measurements," *Remote Sens. Environ.*, vol. 143, pp. 180–191, Mar. 2014, doi: [10.1016/j.rse.2013.12.017](https://doi.org/10.1016/j.rse.2013.12.017).
- [34] S. V. Samsonov and N. d'Oreye, "Multidimensional small baseline subset (MSBAS) for two-dimensional deformation analysis: Case study Mexico City," *Can. J. Remote Sens.*, vol. 43, no. 4, pp. 318–329, Jul. 2017, doi: [10.1080/07399220.2017.1344926](https://doi.org/10.1080/07399220.2017.1344926).
- [35] A. M. Booth et al., "Landslide velocity, thickness, and rheology from remote sensing: La Clapière landslide, France," *Geophys. Res. Lett.*, vol. 40, no. 16, pp. 4299–4304, Aug. 2013, doi: [10.1002/grl.50828](https://doi.org/10.1002/grl.50828).
- [36] X. Hu et al., "Combining InSAR and GPS to determine transient movement and thickness of a seasonally active low-gradient translational landslide," *Geophys. Res. Lett.*, vol. 45, no. 3, pp. 1453–1462, Feb. 2018, doi: [10.1002/2017GL076623](https://doi.org/10.1002/2017GL076623).
- [37] M. Zemp et al., "Global glacier change bulletin no. 5 (2020–2021)," World Glacier Monitoring Service, vol. 5, Jul. 2023, doi: [10.5167/uzh-239577](https://doi.org/10.5167/uzh-239577).

- [38] D. Farinotti et al., "A method to estimate the ice volume and ice-thickness distribution of alpine glaciers," *J. Glaciol.*, vol. 55, no. 191, pp. 422–430, Jan. 2009, doi: [10.3189/002214309788816759](https://doi.org/10.3189/002214309788816759).
- [39] M. A. Werder et al., "A Bayesian ice thickness estimation model for large-scale applications," *J. Glaciol.*, vol. 66, no. 255, pp. 137–152, Feb. 2020, doi: doi: [10.1017/jog.2019.93](https://doi.org/10.1017/jog.2019.93).
- [40] B. G. Delbridge et al., "Three-dimensional surface deformation derived from airborne interferometric UAVSAR: Application to the Slumgullion Landslide," *J. Geophys. Res. Solid Earth*, vol. 121, no. 5, pp. 3951–3977, Apr. 2016, doi: [10.1002/2015JB012559](https://doi.org/10.1002/2015JB012559).
- [41] H. Seroussi et al., "Ice flux divergence anomalies on 79north Glacier, Greenland," *Geophys. Res. Lett.*, vol. 38, no. 9, May 2011, Art. no. L09501, doi: [10.1029/2011GL047338](https://doi.org/10.1029/2011GL047338).
- [42] P. Gantayat, A. V. Kulkarni, and J. Srinivasan, "Estimation of ice thickness using surface velocities and slope: Case study at Gangotri Glacier, India," *J. Glaciol.*, vol. 60, no. 220, pp. 277–282, Jan. 2014, doi: [10.3189/2014JoG13J078](https://doi.org/10.3189/2014JoG13J078).
- [43] A. Linsbauer, F. Paul, and W. Haeberli, "Modeling glacier thickness distribution and bed topography over entire mountain ranges with GlabTop: Application of a fast and robust approach," *J. Geophys. Res. Earth Surf.*, vol. 117, Sep. 2012, Art. no. F03003, doi: [10.1029/2011JF002313](https://doi.org/10.1029/2011JF002313).
- [44] L. Chang and R. F. Hanssen, "A probabilistic approach for InSAR time-series postprocessing," *IEEE Trans. Geosci. Remote Sens.*, vol. 54, no. 1, pp. 421–430, Jan. 2016, doi: [10.1109/TGRS.2015.2459037](https://doi.org/10.1109/TGRS.2015.2459037).
- [45] H. Luo, Q. Xu, Y. Jiang, and C. Pu, "3-D flow velocity time-series analysis from SAR-derived datasets towards maritime glaciers in the Namcha Barwa, Southeastern Tibetan Plateau," *J. Hydrol.*, vol. 635, May 2024, Art. no. 131190, doi: [10.1016/j.jhydrol.2024.131190](https://doi.org/10.1016/j.jhydrol.2024.131190).
- [46] I. M. Howat et al., "Dynamic controls on glacier basal motion inferred from surface ice motion," *J. Geophys. Res. Earth Surf.*, vol. 113, Sep. 2008, Art. no. F03003, doi: [10.1029/2007JF000925](https://doi.org/10.1029/2007JF000925).
- [47] M. P. Bishop et al., "Remote-sensing science and technology for studying glacier processes in high Asia," *Ann. Glaciol.*, vol. 31, pp. 164–170, Sep. 2017, doi: [10.3189/172756400781820147](https://doi.org/10.3189/172756400781820147).



**Liye Yang** received the Ph.D. degree in surveying and mapping engineering from Chang'an University, Xi'an, China, in 2024.

She is currently a Lecturer with Xiangtan University. Her current research interests include the interferometric synthetic aperture radar technique and its applications in the field of glaciers, glacial lakes, and landslides in high-mountainous areas.



**Zhong Lu** (Senior Member, IEEE) received the B.S. and M.S. degrees in geophysics from Peking University, Beijing, China, in 1989 and 1992, respectively, and the Ph.D. degree in geophysics from the University of Alaska, Fairbanks, AK, USA, in 1996.

He is currently a Professor and the Endowed Shuler-Foscue Chair with the Huffington Department of Earth Sciences, Southern Methodist University, Dallas, TX, USA. He is also a Principal Investigator of projects funded by NASA, ESA, JAXA, DLR, and USGS on the study of land surface deformation using satellite interferometric synthetic aperture radar (InSAR) imagery. He has authored more than 45 and coauthored 90 peer-reviewed journal articles and book chapters focused on InSAR techniques and applications. His research interests include technique developments of SAR, InSAR, and their applications on natural hazard monitoring and natural resource characterization.



**Chaoying Zhao** (Senior Member, IEEE) received the M.S. and Ph.D. degrees in geodesy and surveying engineering from Chang'an University, Xi'an, China, in 2002 and 2009, respectively.

He is currently a Professor of geodesy and survey engineering with Chang'an University. His research interests include the development of different InSAR methods, including dynamic SAR/InSAR data processing with the sequential least-squares norm, large gradient surface deformation with SAR offset tracking method, and their applications in geohazard identification, monitoring, and mechanism explanations, including land subsidence, ground fissures, landslide, and mining-induced collapse.



**Xie Hu** (Senior Member, IEEE) received the Bachelor's degree in geographic information system from the China University of Geosciences, Wuhan, China, in 2011, the M.Eng. degree in photogrammetry and remote sensing from Wuhan University, Wuhan, and the Dr. Phil. degree in geophysics from Southern Methodist University, Dallas, TX, USA, in 2018.

She was a Postdoctoral Research Fellow with the University of California, Berkeley, Berkeley, CA, USA, from 2018 to 2020. She is currently an Assistant Professor with Peking University, Beijing, China. Her research interests include SAR remote sensing techniques and applications in geological hazards and the Earth's shallow processes.



**Baohang Wang** received the M.S. and Ph.D. degrees in geodesy and surveying engineering from Chang'an University, Xi'an, China, in 2015 and 2022, respectively.

He is currently a Lecturer of geodesy and survey engineering with the College of Geography and Oceanography, Minjiang University, Fuzhou, China. His research interests include the development of different InSAR methods, including spatiotemporal phase optimization, phase unwrapping, and SAR/InSAR deformation time series updating for artificial infrastructure facilities, land subsidence, and landslide.

artificial